

# 1 **Simulation of electron transport in electron-beam-induced deposition** 2 **of nanostructures**

3 Francesc Salvat-Pujol<sup>\*1</sup>, Harald O. Jeschke<sup>1</sup> and Roser Valentí<sup>1</sup>

4 Address: <sup>1</sup>Institut für Theoretische Physik, Goethe-Universität Frankfurt, Max-von-Laue-Straße 1,  
5 60438 Frankfurt am Main, Germany

6 Email: Francesc Salvat-Pujol - salvat-pujol@itp.uni-frankfurt.de

7 \* Corresponding author

## 8 **Abstract**

9 We present a numerical investigation of energy and charge distributions during electron-beam-  
10 induced growth of W nanostructures on SiO<sub>2</sub> substrates using Monte Carlo simulation of elec-  
11 tron transport. This study gives a quantitative insight into the deposition of energy and charge in  
12 the substrate and in already existing metallic nanostructures in the presence of the electron beam.  
13 We analyze electron trajectories, inelastic mean free paths, and distribution of backscattered elec-  
14 trons in different deposit compositions and depths. We find that, while in the early stages of the  
15 nanostructure growth a significant fraction of electron trajectories still interact with the substrate,  
16 as the nanostructure becomes thicker the transport takes place almost exclusively in the nanostruc-  
17 ture. In particular, a larger deposit density leads to enhanced electron backscattering. This work  
18 shows how mesoscopic radiation-transport techniques can contribute to a model which addresses  
19 the multi-scale nature of the electron-beam-induced deposition (EBID) process. Furthermore, sim-  
20 ilar simulations can aid in understanding the role played by backscattered electrons and emitted  
21 secondary electrons in the change of structural properties of nanostructured materials during post-  
22 growth electron-beam treatments.

## 23 **Keywords**

24 (F)EBID, Monte Carlo simulation of electron transport, electron backscattering, PENELOPE.

## 25 **Introduction**

26 Electron-beam-induced deposition (EBID) [1-3] is a method suitable for template-free fabrica-  
27 tion of nanostructures. Molecules of a precursor gas are injected into a high- or ultra-high-vacuum  
28 chamber and are dissociated by a 1-50 keV focussed electron beam into a volatile fragment, which  
29 is evacuated by the vacuum system, and a non-volatile fragment, which is progressively adsorbed  
30 on a substrate, thus leading to the growth of a nanostructure at the focus of the beam. In general,  
31 the obtained deposits exhibit a granular structure consisting of nanometer-sized metal crystallites  
32 which are embedded in an insulating matrix.

33 There are three main interactions that determine the growth of nanostructures in the EBID process:  
34 (1) substrate-precursor interaction, (2) electron-substrate interaction and (3) electron-precursor in-  
35 teraction. In this work we concentrate on the electron-substrate interaction and our results have  
36 some implications for electron-precursor interaction. Existing theories for the EBID process [4]  
37 consist mainly of equations for the deposition rate that can either be solved analytically under sim-  
38 plifying assumptions or in a more general form using Monte Carlo simulations. However, there  
39 is no theory which addresses the multi-scale nature of the EBID process, including microscopic  
40 and mesoscopic length and time scales, from ultra-fast (non-equilibrium processes occurring in  
41 femtoseconds) to relatively slow (growth and relaxation processes requiring nanoseconds or even  
42 microseconds).

43 In this work we focus on the mesoscopic length scale and present a detailed numerical study of the  
44 distribution of energy and charge originating from EBID conditions. The study is not only rele-  
45 vant for EBID, but also as a first step for understanding aspects of other experimental techniques  
46 including, *e. g.*, the effect of backscattered electrons in changing structural properties in direct and  
47 oxygen-assisted electron-beam post-growth nanostructure treatments [26,27]. We consider various  
48 geometric settings as well as materials relevant to EBID nanostructure growth. For our simulations  
49 we use the Monte Carlo code for radiation transport PENELOPE [5], where a statistical set of parti-  
50 cle trajectories are sampled in homogeneous materials. In this context, we provide an overview of  
51 the aspects of EBID nanostructure growth that can be studied in detail from a mesoscopic point of

52 view using well-established radiation-transport simulation techniques for amorphous media [6,7].  
53 Recently, practical Monte Carlo simulations of EBID-nanostructure growth have been reported [8-  
54 11] on the basis of simplified transport models based, *e. g.*, on the Rutherford cross section or on a  
55 plural-scattering scheme whereby the inelastic scattering of electrons in solids is treated in an av-  
56 erage fashion using the continuous slowing-down approximation (in this approximation only the  
57 energy loss per unit path length is respected: energy fluctuations are not captured). In the present  
58 work we sample inelastic interactions in detail, *i.e.*, on a per-interaction basis without employing a  
59 condensed simulation scheme, and we restrict our considerations to the interaction of the primary  
60 electrons with the substrate and the nanostructure at different stages of its growth.

61 The precursor gas we shall consider throughout this study is tungsten hexacarbonyl,  $W(CO)_6$ , and  
62 the corresponding deposits  $W_xC_yO_z$ , *i.e.* amorphous tungsten oxycarbides with varying carbon and  
63 oxygen contents.  $W(CO)_6$  belongs to the class of organometallic compounds that are well estab-  
64 lished for the EBID process [12-14]. It has been studied in detail by mass spectrometry [15-17]  
65 and photoelectron or photoionization spectroscopy [18-20], which yield appearance energies of  
66 ionic fragments as well as approximate internal energy distributions after electron ionization. The  
67 main advantage of using this precursor gas is that the tungsten metal content in the deposits can  
68 be widely varied so as to cover a wide range of electronic properties, from insulating to metallic  
69 [14,21]. Our aim is to determine a spatially resolved picture of the growth conditions created by  
70 the electron beam within and above a  $SiO_2$  substrate as well as within and above  $W_xC_yO_z$  deposits  
71 of various thicknesses.

## 72 **Description of the simulation**

73 The Monte Carlo method for the simulation of radiation transport is a numerical means of solving  
74 the Boltzmann transport equation in an arbitrary geometry. The computer code system PENELOPE  
75 yields trajectories of primary and secondary particles according to state-of-the-art interaction cross  
76 sections on sample geometries constructed by positioning a set of well-defined homogeneous bod-  
77 ies in space. Random trajectories are generated as follows [5]: particles are characterized by their

78 position vector  $\mathbf{r} = (x, y, z)$ , energy  $E$  and a direction-of-flight unit vector  $\mathbf{d} = (u, v, w)$ , where  $u$ ,  $v$ ,  
79 and  $w$  are the direction cosines. A particle trajectory is represented as a series of states  $(\mathbf{r}_n, E_n, \mathbf{d}_n)$   
80 where  $n$  labels the scattering event at  $\mathbf{r}_n$  leading to energy  $E_n$  and direction  $\mathbf{d}_n$  (see Figure 1). Sev-  
81 eral random variables are sampled from their respective probability distribution functions. The  
82 length of the free path to the next collision,  $s$ , is sampled from an exponential distribution with total  
83 mean free path  $\lambda_T$  using a random number  $\xi$  uniformly distributed in the interval  $(0, 1)$ ,

$$84 \quad s = -\lambda_T \ln \xi. \quad (1)$$

85 The interaction type at the new position is sampled as follows. Let us consider interactions of type  
86 A and B, with respective total cross sections  $\sigma_A$  and  $\sigma_B$ . Interactions of type A and B are sampled  
87 with probabilities

$$88 \quad p_A = \frac{\sigma_A}{\sigma_T}, \quad p_B = \frac{\sigma_B}{\sigma_T}, \quad (2)$$

89 respectively, where  $\sigma_T = \sigma_A + \sigma_B$  is the total interaction cross section. The polar scattering angle  $\theta$   
90 and the energy loss  $W$  are sampled from a distribution with azimuthal symmetry,

$$91 \quad p_{A,B}(E; \theta, W) = \frac{2\pi \sin \theta}{\sigma_{A,B}(E)} \frac{d^2 \sigma_{A,B}(E; \theta, W)}{d\Omega dW}. \quad (3)$$

92 Finally, the azimuthal scattering angle is sampled from a uniform random number  $\xi$  as  $\phi = 2\pi\xi$ .

93 The PENELOPE code [5] uses a relatively sophisticated interaction model, devised for energies  
94 above a few hundred eV. Differential cross sections for elastic scattering were calculated with  
95 the state-of-the-art relativistic partial-wave calculation code ELSEPA [22]. Inelastic interactions  
96 are described by means of the plane-wave Born approximation using a schematized generalized-  
97 oscillator-strength model, fitted to reproduce at high energies the stopping power obtained from the  
98 asymptotic Bethe formula.

99 In our study it is convenient to reduce the problem to two spatial dimensions by assuming a ge-

100 ometry with cylindrical symmetry. We perform studies for two classes of sample geometries: (a)  
 101 a 300 nm thick layer of amorphous SiO<sub>2</sub> with density 2.32 g/cm<sup>3</sup> is placed on top of a Si wafer  
 102 of density 2.33 g/cm<sup>3</sup> in order to study the initial conditions of the EBID growth process. We re-  
 103 fer to this sample geometry briefly as the “substrate”. (b) Structures corresponding to intermedi-  
 104 ate EBID deposits are constructed in order to study the conditions for further growth in the EBID  
 105 process, where deposited layers of different thicknesses (from 5 nm to 200 nm) are placed on top  
 106 of the substrate surface, with its density and composition set in accordance with 6 different ex-  
 107 perimentally realized EBID structures [14]. While the composition in terms of atomic percent is  
 108 taken from Ref. [14], the densities were determined in Ref. [21] by predicting approximate crystal  
 109 structures at these given compositions using evolutionary-algorithm-based crystal structure predic-  
 110 tion. The composition and densities of the deposits are given in Table 1. In both cases, a beam of  
 111 5-keV electrons impinges normally on the surface, with a spot size of 20 nm diameter. In practice,  
 112 the electron beam is rastered on the substrate, so that the extension of the deposited nanostructure  
 113 can be larger than the electron-beam spot size. Thus, a radius of 100 nm has been taken for the de-  
 114 posited nanostructure. The linear range of 5 keV electrons in Si and W is about 0.4 μm and 0.1  
 115 μm, respectively. Thus, in order to ensure that virtually no electrons leave the simulation geometry  
 116 through the lateral bounds (direction perpendicular to the incoming direction), a cylinder radius of  
 117 1 μm has been set. See Figure 2 for an illustration.

**Table 1:** Composition of the six amorphous tungsten oxycarbide deposits considered in this study, following Ref. [14] and given in terms of atomic percent (at %). They are sorted by increasing density which was determined in Ref. [21] (see text).

Composition approximant	Density (g/cm <sup>3</sup> )	W (at %)	C (at %)	O (at %)
WC <sub>2.5</sub> O	7.9	22.6	56.0	21.4
WC <sub>3.33</sub> O <sub>0.67</sub>	8.7	19.0	67.1	13.8
WC <sub>1.4</sub> O <sub>0.8</sub>	9.1	31.8	44.4	23.8
WCO <sub>0.71</sub>	10.0	36.9	35.6	27.5
WC <sub>1.33</sub> O <sub>0.67</sub>	10.4	34.0	44.3	21.7
WC <sub>1.75</sub> O <sub>0.75</sub>	10.6	27.5	50.4	22.1

118 Material cross sections in our calculations are approximated as an averaged weighted sum of

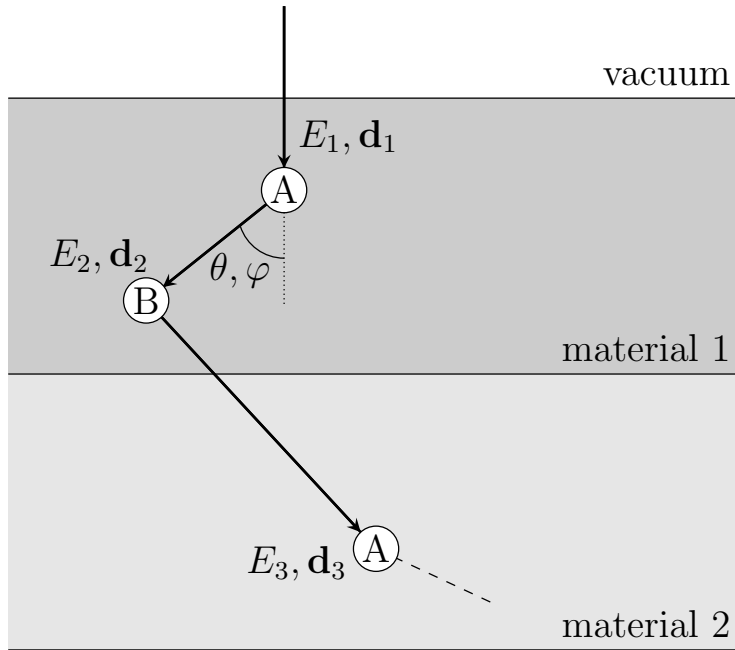


**Figure 1:** Schematic representation of a random trajectory generated by PENELOPE [5]. The trajectory is determined by path lengths  $s$  that determine the position  $\mathbf{r}_n$  of the next scattering event, by the type of event, and by energies  $E_n$  and directions  $\mathbf{d}_n$  after the event.

119 the atomic cross sections corresponding to a given composition (incoherent sum of scattered in-  
 120 tensities), thus neglecting chemical binding effects. Energetic electrons can scatter either elasti-  
 121 cally, where the quantum state of the scatterer remains unaltered and the direction of the projectile  
 122 changes, or inelastically, where electronic excitations or ionizations take place through the different  
 123 energy and momentum transfer channels available. As the electrons evolve through the medium,  
 124 they lose energy in the course of several inelastic interactions. The lost energy is either absorbed by  
 125 the medium through local excitations, which are allowed to relax through the emission of photons,  
 126 or through ionization of the sample, which leads to the build-up of a localized positive charge in  
 127 the material and to new particles, thus leading to a “shower” of particles. If an electron crosses a  
 128 boundary into an adjacent material, its trajectory history is stopped at the other side of the interface  
 129 and restarted with the new material transport properties. This can be done any time, since electron  
 130 trajectories are modelled as Markov processes (the future of the trajectory is dependent only on  
 131 the present state, and not on the past). The trajectory history of an electron is stopped when its en-  
 132 ergy drops below 50 eV: the electron is then considered absorbed by the medium, contributing to

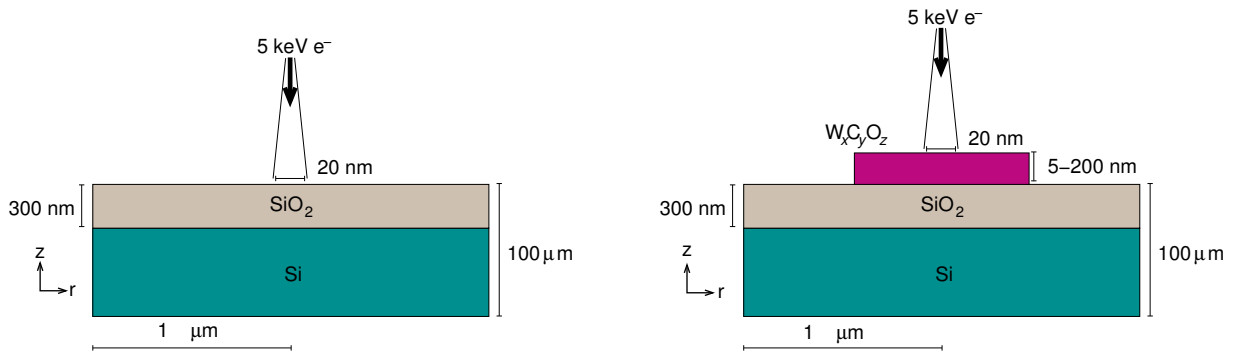


**Figure 2:** Cylindrical sample geometries used in the simulations. Left: A 300 nm thick amorphous SiO<sub>2</sub> substrate is placed above a Si wafer and irradiated with 5 keV electrons. Right: A W<sub>x</sub>C<sub>y</sub>O<sub>z</sub> deposit of thickness from 5 nm to 200 nm and of density and composition as given in Table 1 is placed above a 300 nm amorphous SiO<sub>2</sub> layer, which in turn is placed on top of a Si wafer. A conical electron beam with a spot size of 20 nm on the sample is used, the point source being located 1 cm in vacuum above the center of the sample; the corresponding beam aperture is  $5.73 \times 10^{-5}$  degrees. A radius of 100 nm is chosen for the deposit.

133 the build-up of a localized negative charge in the material. We choose an absorption energy of 50  
 134 eV because we are neglecting binding effects in the material, and furthermore, elastic and inelastic  
 135 cross sections derived from atomistic models carry large uncertainties already for energies below a  
 136 few hundred eV. The same absorption energy is used for those secondary electrons generated in the  
 137 shower. Finally, to obtain our simulated results, we have sampled  $10^8$  trajectories.

## 138 Results

139 To provide a first visual insight into the electron transport process in the substrate and in the de-  
 140 posited nanostructure, Figure 3 displays a simulated shower of 5-keV-electron trajectories imping-  
 141 ing normally on a 500 nm thick slab of SiO<sub>2</sub> (left-hand side, substrate material) and on a 500 nm  
 142 thick slab of pure W (right-hand side, deposit material), respectively. We consider pure tungsten  
 143 as a representative material of the different deposits for practical reasons. This choice is reason-  
 144 able inasmuch as the average distance between consecutive inelastic collisions [inelastic mean  
 145 free path (IMFP)] of electrons in W and in the considered nanostructure materials are very sim-  
 146 ilar in the energy window of interest (see Figure 4). Note that in the SiO<sub>2</sub> substrate the beam is  
 147 completely attenuated at a depth of  $\sim 500$  nm, whereas in W this depth is reduced to  $\sim 150$  nm.

148 Indeed, the IMFP of electrons in  $\text{SiO}_2$  is roughly a factor 2–4 larger than the IMFP of electrons  
 149 in  $W$  (or any of the 6 considered deposit materials), as shown on the left-hand panel of Figure 4.  
 150 Thus, we conclude that in the early stages of the nanostructure growth (thicknesses much smaller  
 151 than  $\sim 150$  nm), the electron beam probes both the thin deposit and the substrate. The energy and  
 152 charge deposition processes are therefore dictated by the transport characteristics of both the de-  
 153 posit and the substrate. On the other hand, for nanostructure thicknesses exceeding  $\sim 150$  nm, the  
 154 deposition of energy and charge takes place almost exclusively in the nanostructure, without af-  
 155 fecting the substrate. A similar analysis has been carried out in Ref. [11]. Experimentally, similar  
 156 conclusions are drawn from current measurements [23].

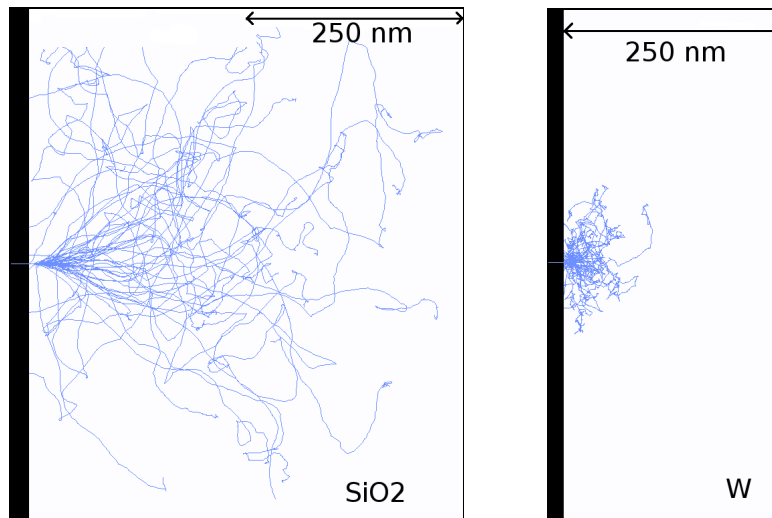


**Figure 3:** Snapshot of 50 simulated electron trajectories in the  $\text{SiO}_2$  substrate (left-hand side) and in the nanostructure deposit material  $W$  (right-hand side, representative for material deposit). The width of the screenshot windows corresponds to 500 nm.

157 Figure 5(a) displays the energy distribution of electrons backscattered and emitted per incoming  
 158 electron from the substrate (darkest curve) and from deposits of increasing thicknesses  $d_{\text{WCO}}$  on  
 159 top of the substrate [dark blue curve,  $d_{\text{WCO}} = 5$  nm, through light blue curve,  $d_{\text{WCO}} = 200$  nm].  
 160 Notice that for thin deposits the spectral features of the substrate are merely smeared out, ow-  
 161 ing to the fact that only few inelastic interactions take place in the thin deposit. For increasing  
 162 deposit thicknesses, the transport in the substrate plays an increasingly marginal role. Thus, for  
 163 thick deposits the spectral features of the substrate vanish and the spectral features of the deposit



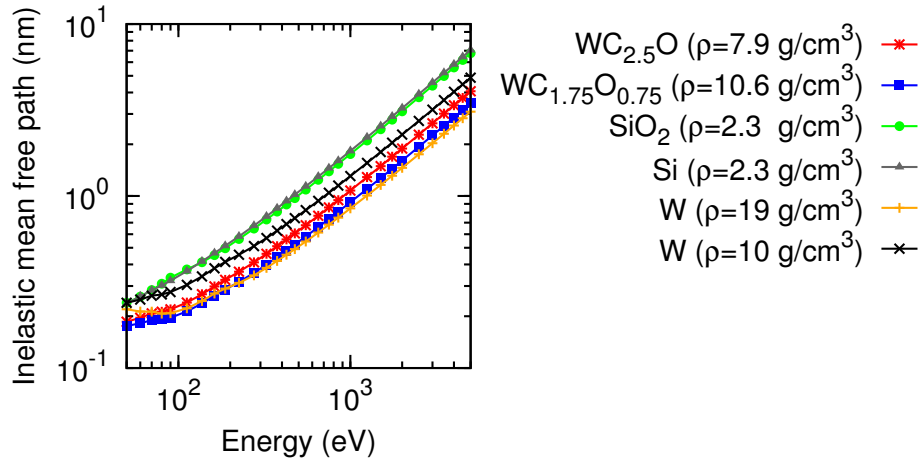


**Figure 4:** Inelastic mean free paths for the relevant materials in this work presented in the usual log-log scale. The tungsten oxycarbide compositions  $WC_{2.5}O$  and  $WC_{1.75}O_{0.75}$  correspond to the lowest and highest density samples of Table 1, respectively. The two curves with cross symbols show the variation due to a density change only.

164 prevail. This explains the saturated behavior of the curves corresponding to  $d_{WCO} = 100$  nm and  
 165  $d_{WCO} = 200$  nm, where electrons are very unlikely to even reach the substrate, in accordance with  
 166 the discussion of Figure 3. It is interesting to note that the intensity in the energy distribution of  
 167 backscattered electrons increases with the sample thickness. Indeed, on the one hand the elastic  
 168 backscattering coefficient increases with the atomic number, leading to the observed increase in  
 169 the elastic peak at 5 keV [the substrate consists of Si and O (atomic numbers  $Z = 14$  and  $Z = 8$ ,  
 170 respectively) whereas the deposit material contains W ( $Z = 74$ )]. On the other hand, the IMFP  
 171 is inversely proportional to the material density, so that a denser deposit on a comparatively light  
 172 substrate implies an increase in the number of energy losses per unit path length with respect to  
 173 those that would take place in the substrate alone. This justifies the factor  $\sim 2$  between the curves  
 174 corresponding to the (thick) deposit and the substrate. Thus, under the assumption that the pres-  
 175 ence of a large number of electrons (slow or fast) enhances the dissociation rate of precursor gas  
 176 molecules adsorbed on the substrate, one can infer the following positive-feedback process: as the  
 177 deposit thickness grows, so does the number of backscattered and emitted electrons, leading to an  
 178 improvement in the dissociation rate and, therefore, in the nanostructure deposition rate, leading  
 179 to a reinforced growth process. A more quantitative description of the change in deposition rate

180 would imply analyzing the separate contributions from backscattered electrons, forward-scattered  
181 electrons, and secondary electrons [24].

182 Two aspects of Figure 5(a) should be emphasized. (1) In order to further elucidate the dependence  
183 of the electron backscattering probability with the atomic number of the deposit material, the sim-  
184 ulation was repeated replacing the deposit with Co, a comparatively lighter material ( $Z = 27$ ). Fig-  
185 ure 5(b) displays the energy distribution of backscattered electrons for different Co-nanodeposit  
186 thicknesses,  $d_{\text{Co}}$ . Notice that the increase in the elastic-peak intensity is roughly a factor 2 or 3  
187 smaller than for the nanostructure material, which is much heavier. (2) Notice that as the deposit  
188 becomes thicker, the intensity of the curves increases monotonically, reaching its maximum for a  
189 thickness of about 50 nm and then decreasing slightly into its saturated value for thicknesses of 200  
190 nm. The fact that multiple elastic and inelastic interactions take place along the trajectory makes  
191 it hard to give a detailed explanation of this effect. Nevertheless, it can be argued that for thick-  
192 nesses exceeding 50 nm, the fraction of trajectories which reach the substrate becomes negligible  
193 and, for thick enough deposits, this fraction approaches zero. Owing to the fact that the mean free  
194 paths in the deposit are much shorter than in the substrate, more energy losses take place per unit  
195 path length in the deposit than in the substrate. This implies that the thicker the deposit becomes,  
196 the larger is the number of electrons which leave the sample after losing most of its energy. This  
197 explains, at least qualitatively, the increase and eventual saturation in the low-energy regime of the  
198 spectrum (contribution of electrons which leave the sample after losing most of its energy and of  
199 emitted secondary electrons), as well as the decrease in intensity in the energy range between 1  
200 and 4 keV (for thick substrate electrons in this regime lose more energy and therefore the spectral  
201 intensity shifts to lower energies). Close to the elastic peak, variations with the thickness of the  
202 substrate between 50 nm and 200 nm are not visible, since the elastic backscattering probability for  
203 the deposit is much larger than for the substrate.

204 The primary energy of the electrons (5 keV) is high enough to produce inner-shell ionizations in  
205 Si and O. Let S0 denote the ionized shell. A second electron from an outer shell, S1, fills the va-  
206 cancy and, subsequently, two processes are possible: (1) a radiative transition whereby a photon

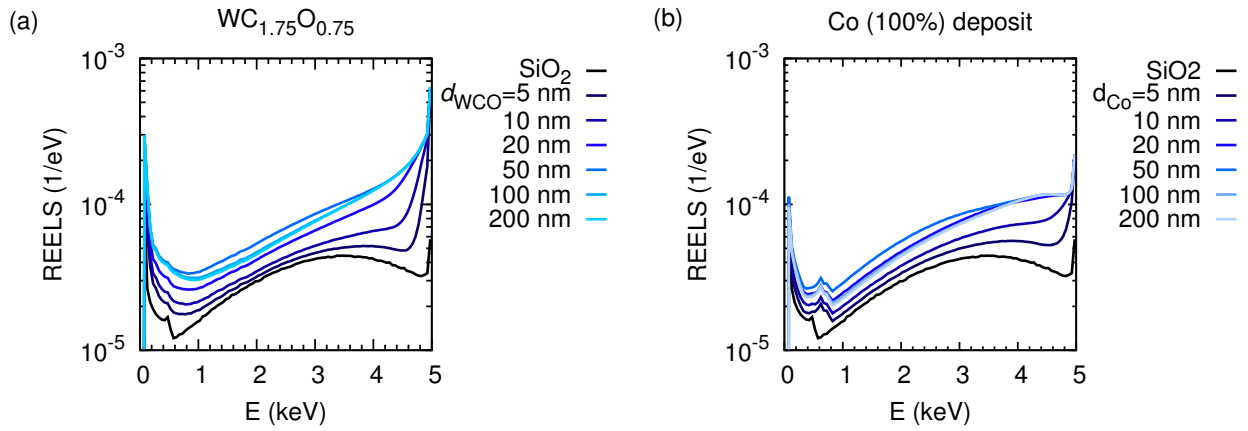


**Figure 5:** (a) Distribution of electrons backscattered and emitted into the vacuum from the substrate in absence of a deposit (black curve) and from the substrate with a deposit of thickness  $d_{\text{WCO}}$  ranging from 5 nm to 200 nm (rest of curves) consisting of the material corresponding to the composition  $\text{WC}_{1.75}\text{O}_{0.75}$  (see Table 1). (b) Same as panel (a) for a deposit of pure Co. Notice that the ordinates are in a logarithmic scale, whereas the abscissas are in a linear scale. The acronym REELS stands for reflection electron-energy-loss spectrum.

207 is emitted with a characteristic energy  $U_{S_0} - U_{S_1}$ , where  $U$  denotes the ionization energy of the  
 208 corresponding shell, or (2), typically more likely, a non-radiative transition whereby an electron  
 209 from an outer shell  $S_2$  (which can either coincide with or be less bound than  $S_1$ ) is emitted as an  
 210 Auger electron with energy  $U_{S_0} - U_{S_1} - U_{S_2}$ . The emitted photons might either leave the sample  
 211 or be absorbed by a target atom, leading to photoelectron emission. Figure 6 displays the distribu-  
 212 tion of electrons (solid red curve) and photons (dashed blue curve) emitted from the substrate per  
 213 incoming electron in the absence of a deposit. The peaks in the photon spectrum, superimposed  
 214 on a bremsstrahlung background, correspond to K lines of Si and O, situated at 1739–1835 eV and  
 215 523 eV, respectively. Notice that the number of photons emitted per incoming electron is at least  
 216 two orders of magnitude smaller than the number of emitted electrons. Furthermore, interaction  
 217 mean free paths for photons are typically much longer than for electrons. Thus, the contribution of  
 218 the emitted photons to the energy and charge deposition processes is presumably negligible, except  
 219 for the minor photoelectron peak in the electron spectrum of the substrate at 500 eV, superimposed  
 220 to a contribution from Auger electron emission from O with energies from 478.8 eV to 508.9 eV.  
 221 A contribution of Auger- or photoelectrons is not observed at 1739 – 1835 eV, because (1) Auger-  
 222 electron energies are spread over a few hundred eV and thus do not lead to a well resolved peak

223 and (2) the photoelectric cross section at these energies one order of magnitude smaller than at 500  
 224 eV (cross section data taken from the numerical database of PENELOPE [5]). The photon spectrum  
 225 was also examined when a deposit lies on the substrate without finding significant deviations re-  
 226 garding the minor role played by photon transport as demonstrated for the pure substrate.

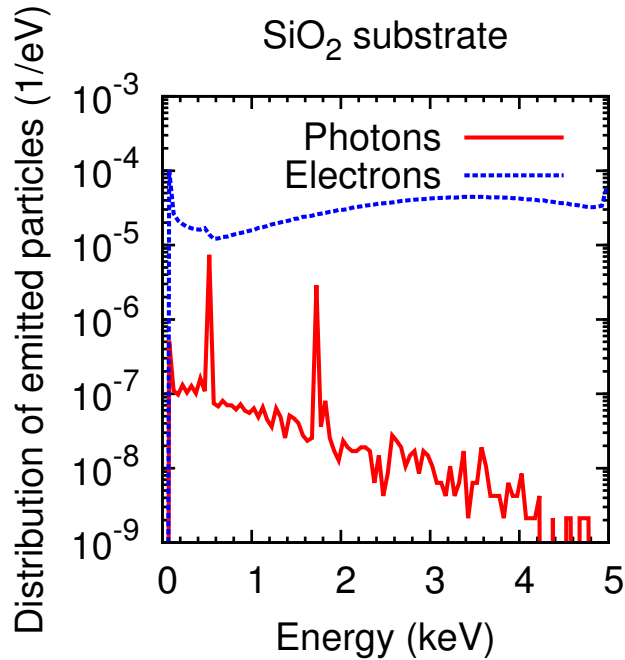


**Figure 6:** Distribution of electrons backscattered and emitted into the vacuum from the substrate in the absence of a deposit (dashed curve) and distribution of photons emitted into the vacuum (solid curve). Note, that the ordinates are in a logarithmic scale, whereas the abscissas are in a linear scale.

227 Figure 7 displays the distribution of energy deposited in the system as a function of depth for sam-  
 228 ple thicknesses  $d_{\text{WCO}}$  ranging from 10 nm to 200 nm. Negative depths correspond to the  $\text{SiO}_2$   
 229 substrate, whereas positive depths denote the deposit, indicated respectively by the magenta and  
 230 grey bars (reflecting the color code in Figure 2). The black solid and the dashed red curve corre-  
 231 spond to  $\text{WC}_{2.5}\text{O}$  (lowest density sample) and  $\text{WC}_{1.75}\text{O}_{0.75}$  (highest density sample), respectively.  
 232 The panel corresponding to  $d_{\text{WCO}} = 200$  nm additionally shows the deposited energy for samples  
 233 with intermediate values of the density. It is clear that the deposited energy per unit depth is much  
 234 higher in the deposit than in the substrate, since the IMFP is a factor  $\sim 2$  shorter in the deposit than

235 in the substrate, and thus energy-loss events take place more often in the deposit than in the sub-  
 236 strate. This also explains the discontinuous jump at the deposit-substrate interface.

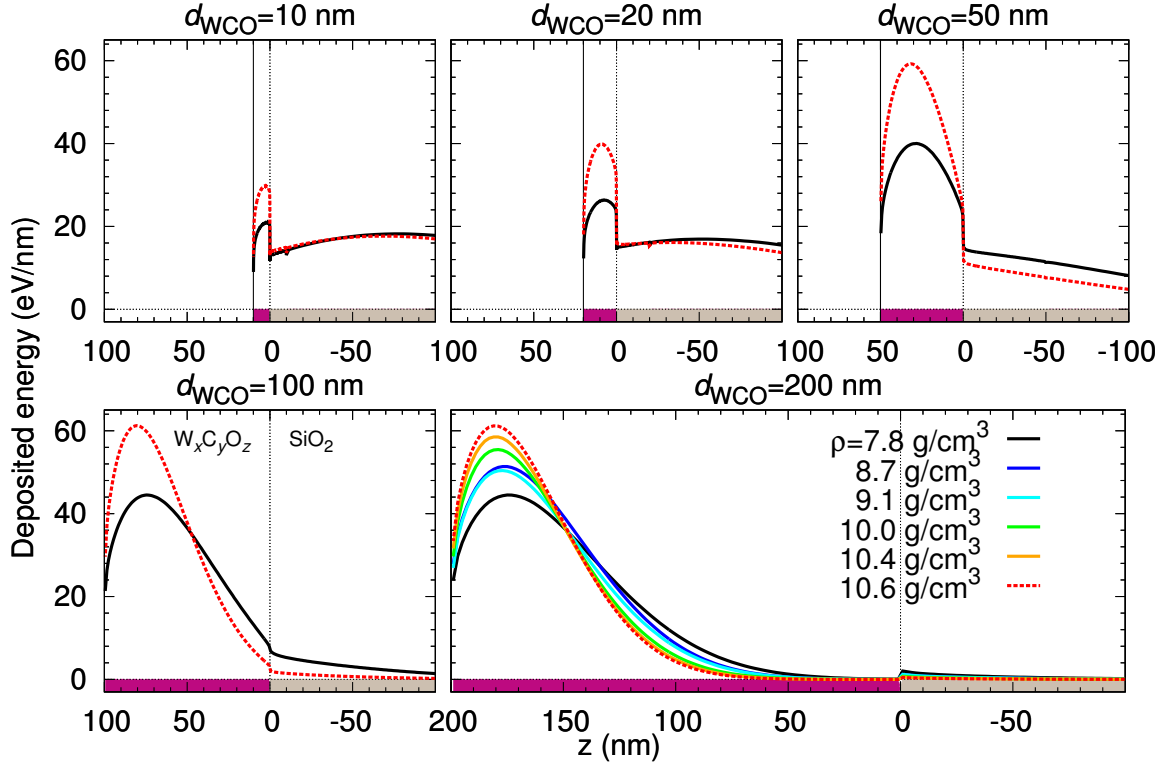


**Figure 7:** Energy deposited in the system as a function of the depth  $z$  for the indicated sample thicknesses  $d_{\text{WCO}}$  and for the six nanostructure materials specified in Table 1. The position  $z = 0$  corresponds to the deposit-substrate interface; the position  $z = d_{\text{WCO}}$  (indicated by a solid vertical line in the three upper panels) corresponds to the deposit-vacuum interface. Notice that, in addition to the density, the composition of the samples varies (see Table 1).

237 It should be noted that, whereas the density increases linearly from  $\text{WC}_{2.5}\text{O}$  to  $\text{WC}_{1.75}\text{O}_{0.75}$ , the  
 238 tungsten content does not exhibit a clear trend (see Table 1). In order to separately exhibit the ef-  
 239 fect of density and W-content variations on the distribution of deposited energy, we have consid-  
 240 ered the following artificial material variations. On the one hand, we have taken a sample with a  
 241 fixed density  $\rho = 10.6092$  g/cm<sup>3</sup> (corresponding to  $\text{WC}_{1.75}\text{O}_{0.75}$ ) and have varied its W content  
 242 from 17.5% to 37.5% in steps of 2.5% (covering the range of W contents in Table 1), decreasing  
 243 both the C and the O contents by 1.25% at each step. We have also considered the extreme case of  
 244 100% W content. The distribution of deposited energy as a function of depth is shown in Figure 8  
 245 and the corresponding IMFPs are displayed in Figure 9. On the other hand, we have taken a sam-

246 ple with a fixed W content (27.5% W, 50.4% C, 22.1% O, corresponding to  $WC_{1.75}O_{0.75}$ ) and have  
 247 varied its density from  $8 \text{ g/cm}^3$  to  $12 \text{ g/cm}^3$  (covering the range of densities given in Table 1). The  
 248 distribution of deposited energy and the corresponding IMFPs are shown in Figures 10 and 11, re-  
 249 spectively. Comparing Figures 8 and 10 we conclude that variations in the density influence the en-  
 250 ergy deposition process in the nanostructure much more strongly than variations in the W content  
 251 (in the considered variation intervals of these parameters). This can be best observed in the case of  
 252 sample thickness  $d_{WCO} = 200 \text{ nm}$  for  $z = 50$  to  $150 \text{ nm}$ .

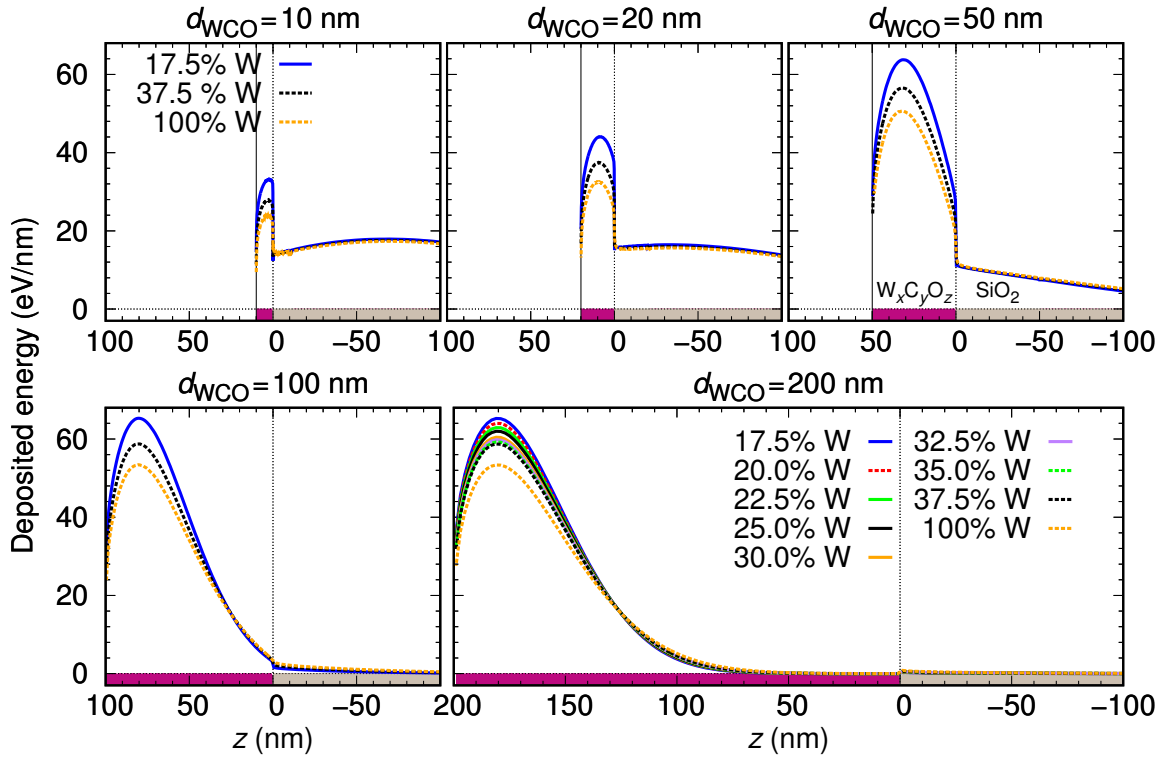


**Figure 8:** Same as Figure 7 for a fixed deposit density ( $\rho = 10.6092 \text{ g/cm}^3$ ) and variable tungsten content.

253 In practice, sample charging effects in the EBID process cause only a minor repulsion of the elec-  
 254 tron beam (observed as a slight drift in the monitoring images) which can be easily corrected by  
 255 applying appropriate beam-deflection voltages. Nevertheless it is interesting *per se* to examine the  
 256 spatial distribution of the charge deposition process induced by the incoming beam, if only to bet-  
 257 ter delimit the spatial region that is probed and affected by the beam. Figure 12 displays the distri-  
 258 bution of charge deposited per unit path length for deposit thicknesses  $d_{WCO}$  ranging from 10 nm

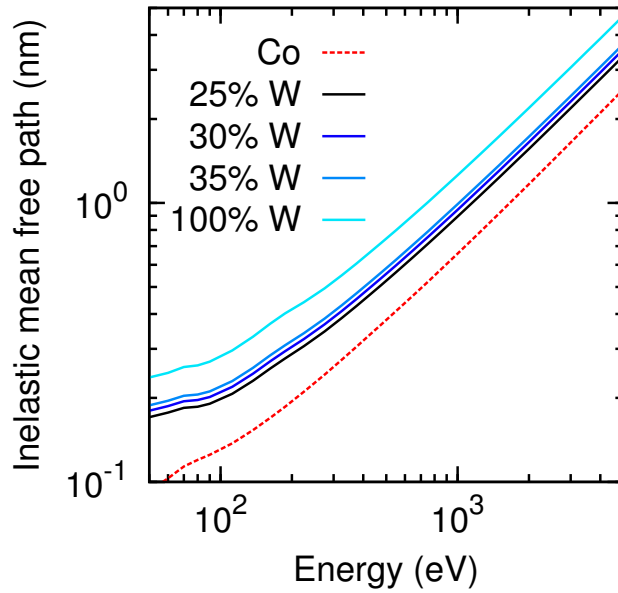


**Figure 9:** IMFP in the different deposits with fixed density ( $\rho = 10.6092 \text{ g/cm}^3$ ) and variable tungsten content.

259 to 200 nm in  $\text{WC}_{2.5}\text{O}$  and  $\text{WC}_{1.75}\text{O}_{0.75}$  (solid black and dashed red line, respectively). Calcula-  
 260 tions were also carried out for samples of intermediate densities but are not shown in the Figure,  
 261 which displays only the two extreme cases for clarity. Note, that the charge deposited in the nanostruc-  
 262 ture close to the vacuum interface is positive. This implies that there are more secondary elec-  
 263 trons emitted from this region than slow electrons absorbed in it. Indeed, those secondary electrons  
 264 emitted from the nanostructure into the vacuum do not return, implying that close to the vacuum  
 265 interface it is more likely to see a lack of electrons than the absorption of slow electrons. Deeper  
 266 into the nanostructure, the absorption of slow electrons becomes more likely: secondary electrons  
 267 are more likely to become absorbed than to reach the interface into vacuum. This leads to the ob-  
 268 served decrease in the deposited charge, which becomes even negative when the nanostructure is  
 269 thick enough so that all generated secondary electrons are eventually absorbed in it. Regarding  
 270 the deposit-substrate interface, two aspects should be considered. On the one hand, the primary  
 271 electron loses less energy in the  $\text{SiO}_2$  substrate than in the nanostructure material, so that less sec-  
 272 ondary electrons are generated per unit path length in the substrate. On the other hand, secondary  
 273 electrons from the nanostructure cross the interface into the substrate. The number of slow elec-  
 274 trons moving from the nanostructure into the substrate is larger than the number of slow electrons

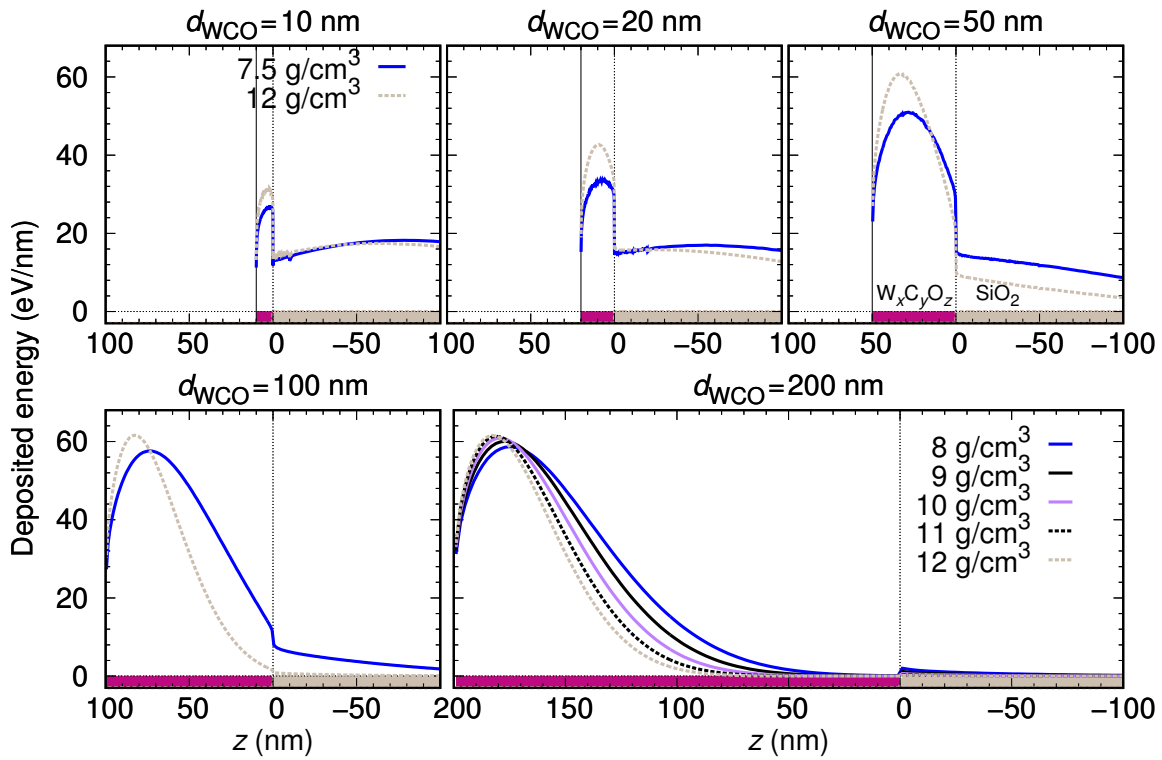


**Figure 10:** Same as Figure 7 for a fixed composition (27.5% W, 50.4% C, 22.1% O) and variable density.

275 moving in the opposite direction. This leads to the observed increase in positive (negative) charge  
 276 in the nanostructure (substrate) side of the interface.

277 Finally, Figures 13 and 14 display, respectively, the distribution of deposited energy and charge  
 278 as a function of the depth and the radial coordinate in  $WC_{1.75}O_{0.75}$  (highest density sample) for  
 279 nanostructure thicknesses of 10 and 100 nm. The panels in the right-hand side show cross sections  
 280 of the distributions at the indicated depths  $z$ . In these figures one can clearly identify the beam ra-  
 281 dius of 10 nm. Notice that at radii  $r < 10$  nm the deposited charge is positive. In this region, sec-  
 282 ondary electrons are emitted as a result of the energy loss of the primary electrons. For distances  
 283  $r > 10$  nm, the deposited charge is negative, meaning that electrons with  $E \leq 50$  eV are absorbed  
 284 there. These slow electrons are those secondary electrons generated in  $r < 10$  nm which wander  
 285 into  $r > 10$  nm and are not able to travel further, being absorbed.

286 The distribution of deposited energy as a function of the depth and of the radial coordinate has ad-  
 287 ditional value. On the one hand, it can be used to derive a temperature distribution for more de-



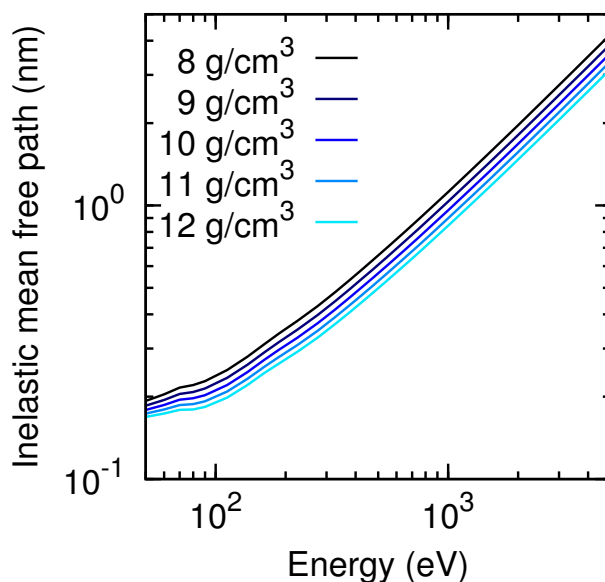


**Figure 11:** IMFP in different deposits with fixed composition (27.5% W, 50.4% C, 22.1% O) and variable density.

288 tailed microscopic simulations (*e.g.* molecular dynamics) of the EBID process [25]. On the other  
 289 hand, the deposited energy also contributes to an enhancement of the dissociation of precursor gas  
 290 molecules adsorbed on the surface. It is therefore worthwhile to have an accurate estimate for this  
 291 quantity. The consequences for nanostructure growth are an interesting topic of further research.

## 292 Conclusions

293 In this work we presented results of Monte Carlo simulations of electron transport which provide  
 294 valuable insight into the charge and energy deposition processes induced by the primary electron  
 295 beam in the EBID process of  $W(CO)_6$  nanostructures on  $SiO_2$  substrates. The simulations high-  
 296 light the differences in the transport of electrons in the nanostructure and in the substrate: the mean  
 297 free path between consecutive inelastic interactions in the deposit is a factor  $\sim 2$  smaller than in  
 298 the substrate which leads to a beam attenuation after a depth of  $\sim 500$  nm in the substrate mate-  
 299 rial, whereas, in the nanostructure material, the beam is attenuated at much shallower depths of  
 300  $\sim 150$  nm. In the early stages of the nanostructure growth (thickness well below 150 nm), a sig-  
 301 nificant fraction of incoming electron trajectories still interact with the substrate. As the nanos-  
 302 tructure becomes thicker ( $\gtrsim 100$  nm), the transport takes place almost exclusively in the nanos-

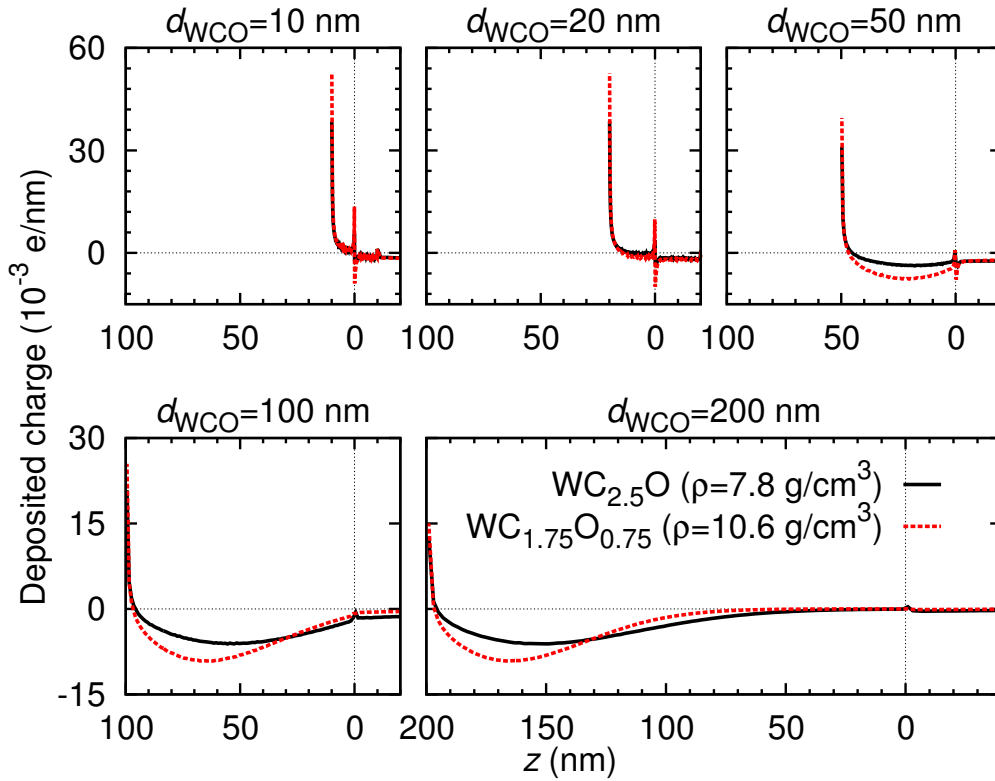


**Figure 12:** Charge deposited into the system as a function of the depth  $z$  for the indicated sample thicknesses  $d_{\text{WCO}}$  and for the six nanostructure materials specified in Table 1 (compare with Figure 7).

303 structure, leading to a saturated behavior of the distribution of the deposited energy, charge, and  
 304 backscattered electrons. The simulations show two effects which may be important for the growth  
 305 of the nanostructure. (1) The energy deposited in the substrate is available for the dissociation of  
 306 precursor-gas molecules adsorbed on the surface substrate. (2) If we assume that a larger yield of  
 307 secondary electrons enhances precursor dissociation and improves the conditions for nanodeposit  
 308 growth with high density and metal content, then the simulations show that larger deposit density  
 309 leads to enhanced electron backscattering. This implies that random fluctuations in deposit density  
 310 could be amplified through positive feedback.

311 The presented simulations therefore provide an overview of the effect of the primary-electron beam  
 312 on the deposit and on the substrate at different stages of the nanostructure growth. Furthermore,  
 313 the distributions of deposited energy serve as a starting point for further microscopic simulations  
 314 (molecular dynamics) in that they provide a guideline for the initial temperature distribution in the

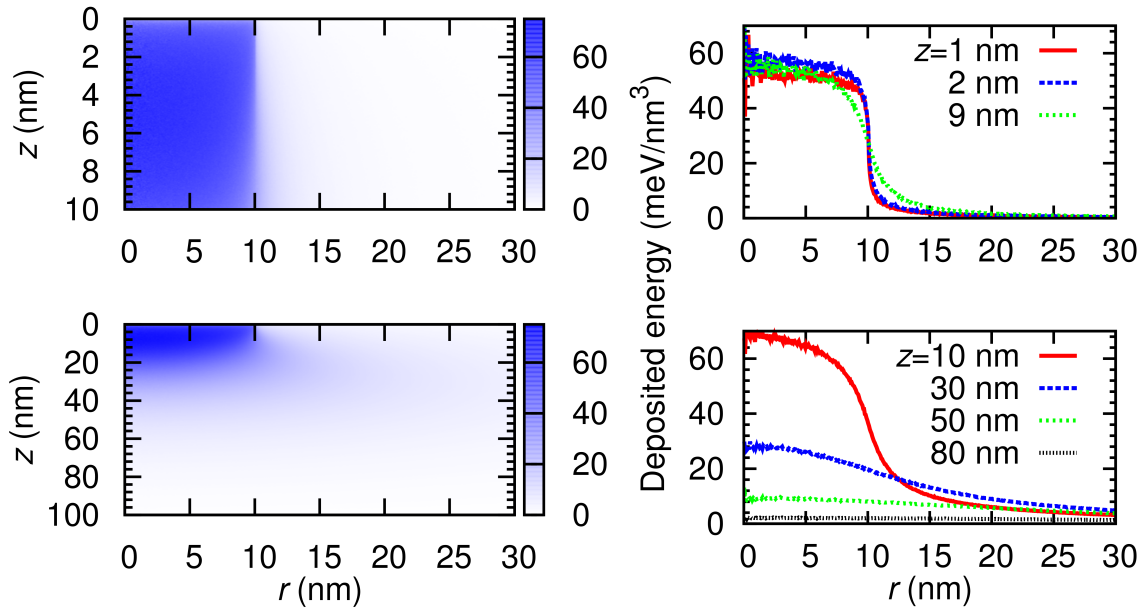


**Figure 13:** Distribution of energy deposited in  $\text{WC}_{1.75}\text{O}_{0.75}$  as a function of the depth  $z$  and the radial coordinate  $r$ . The two upper (lower) panels correspond to a sample thickness  $d_{\text{WCO}} = 10$  nm ( $d_{\text{WCO}} = 100$  nm). The right-hand-side panels display cross sections of the distribution at the indicated depths  $z$  below the deposit-vacuum interface.

315 substrate and the deposit under irradiation with an electron beam. Moreover, similar simulations  
 316 can aid in understanding the role played by backscattered and secondary electrons in changing  
 317 structural properties of nanostructured materials in several post-growth techniques, including di-  
 318 rect or oxygen-assisted electron-beam curing [26,27].

### 319 Acknowledgements

320 We are indebted to Prof. Francesc Salvat of the Universitat de Barcelona for the very fruitful dis-  
 321 cussions and we acknowledge the contribution of Carlos Ortiz at the beginning of this work. Fund-  
 322 ing by the Beilstein-Institut is gratefully acknowledged.

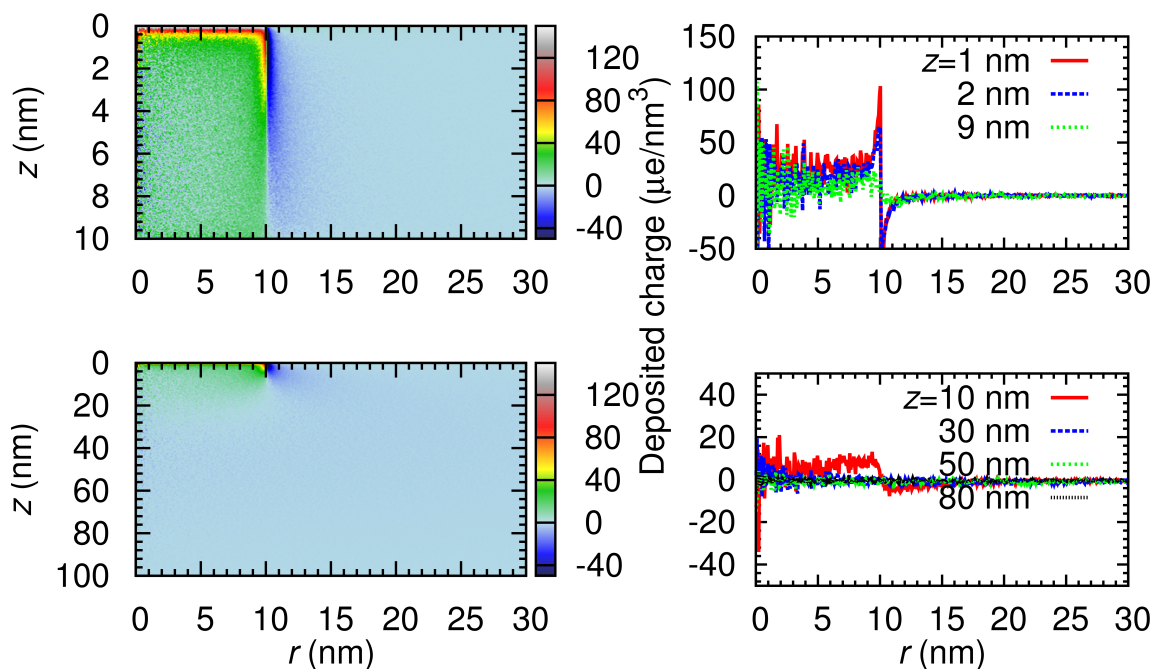


**Figure 14:** Same as Figure 13 for the charge deposited in  $WC_{1.75}O_{0.75}$ .

## References

323

324

1. Koops, H.; Kretz, J.; Rudolph, M.; Weber, M. *J. Vac. Sci. Technol.* **1993**, *11*, 2386.

325

2. Randolph, S.; Fowlkes, J.; Rack, P. *CRC Cr. Rev. Sol. State* **2006**, *31*, 55.

326

3. Utke, I.; Hoffmann, P.; Melngailis, J. *J. Vac. Sci. Technol. B* **2008**, *26* (4), 1197.

327

4. Huth, M.; Porrati, F.; Schwalb, C.; Winhold, M.; sachser, R.; Dukic, M.; Adams, J.; Fantner, G. *Beilstein J. Nano.* **2012**, *3*, 597–619.

328

329

5. Salvat, F.; Fernández-Varea, J. M.; Sempau, J. *PENELOPE-2011: A code System for Monte Carlo Simulation of Electron and Photon Transport*; OECD/NEA Data Bank: Issy-les-Moulineaux, France, 2011. Available in PDF format from <http://www.nea.fr/lists/penelope.html>.

330

331

332

333

6. Joy, D. *Monte Carlo modelling for Electron Microscopy and Microanalysis*; Oxford University Press, 1995.

334

335

7. Lin, Y.; Joy, D. C. *Surf. Interface Anal.* **2005**, *37*, 895–900.

- 336 8. Liu, Z. Q.; Mitsuishi, K.; Furuya, K. *Nanotechnology* **2005**, *17*, 3832–3837.
- 337 9. Silvis-Cividjian, N.; Hagen, C. W.; Leunissen, L. H.; Kruit, P. *Microelectron. Eng.* **2002**, *61–*  
338 *62*, 693–699.
- 339 10. Smith, D. A.; Fowlkes, J. D.; Rack, P. D. *Nanotechnology* **2007**, *18*, 265308.
- 340 11. Smith, D. A.; Fowlkes, J. D.; Rack, P. D. *Small* **2008**, *4* (9), 1382–1389.
- 341 12. Hoyle, P. C.; Ogasawara, M.; Cleaver, J. R. A.; Ahmed, H. *Appl. Phys. Lett.* **1993**, *62* (23),  
342 3043–3045.
- 343 13. Hoyle, P. C.; Cleaver, J. R. A.; Ahmed, H. *J. Vac. Sci. Technol. B* **1996**, *14* (2), 662.
- 344 14. Huth, M.; Klingenberger, D.; Grimm, C.; Porrati, F.; Sachser, R. *New J. Phys* **2009**, *11*,  
345 033032.
- 346 15. Beranova, S.; Wesdemiotis, C. *J. Am. Soc. Mass Spectr.* **1994**, *5* (12), 1093–1101.
- 347 16. Cooks, R. G.; Ast, T.; Klraj, B.; Kramer, V.; Igon, D. Z. *J. Am. Soc. Mass Spectr.* **1990**, *1* (1),  
348 16–27.
- 349 17. Michels, G. D.; Flesch, G. D.; Svec, H. J. *Inorg. Chem.* **1980**, *19* (2), 479–485.
- 350 18. Cooper, G.; Green, J. C.; Payne, M. P.; Dobson, B. R.; Hillier, I. H. *J. Am. Chem. Soc.* **1987**,  
351 *109* (13), 3836–3842.
- 352 19. Hubbard, J. L.; Lichtenberger, D. L. *J. Am. Chem. Soc.* **1982**, *104* (8), 2132–2138.
- 353 20. F., Q.; S., Y. *J. Chem. Phys.* **1997**, *107* (24), 10391–10398.
- 354 21. Muthukumar, K.; Valentí, R.; Jeschke, H. O. *New J. Phys* **2012**, *14*, 113028.
- 355 22. Salvat, F.; Jablonski, A.; Powell, C. J. *Comput. Phys. Commun.* **2005**, *165*, 157–190.
- 356 23. Bret, T.; Utke, I.; Bachmann, A.; Hoffmann, P. *Appl. Phys. Lett.* **2003**, *83*, 4005–4007.

- 357 24. Plank, H.; Smith, D. A.; Haber, T.; Rack, P. D.; Hofer, F. *ACS Nano* **2012**, *6* (1), 286–294.
- 358 25. Randolph, S. J.; Fowlkes, J. D.; Rack, P. D. *J. Appl. Phys.* **2005**, *97*, 124312.
- 359 26. Porrati, F.; Sachser, R.; Schwalb, C. H.; Frangakis, A. S.; Huth, M. *J. Appl. Phys.* **2011**, *109*,  
360 063715.
- 361 27. Mehendale, S.; Mulders, J. J. L.; Trompenaars, P. H. F. **2013**, *24*, 145303.